nature water

Article

https://doi.org/10.1038/s44221-025-00544-2

Iminodiacetic acid modification enables nanopore identification of major divalent metal ions in natural water samples

Received: 9 May 2025

Accepted: 29 October 2025

Published online: 6 January 2026

Check for updates

Wen Sun[1,2], Tian Li[1,2], Zixuan Wang[1,2], Yunqi Xiao[1,2], Panke Zhang[1], Kefan Wang[1,2] & Shuo Huang[1,2]

Metal elements, critical to diverse industrial applications, also pose substantial environmental pollution risks when mismanaged. Conventional metal ion detection methods, however, are limited by high operational costs, bulky equipment and poor portability for on-site analysis, suggesting the need for an accurate, cost-effective and portable sensing strategy that is capable of addressing various metal ions directly from a heterogeneous sample. In this study, we engineered a *Mycobacterium smegmatis* porin A nanopore by incorporating an iminodiacetic acid ligand at its constriction site, creating a versatile sensor that is capable of simultaneously identifying ten divalent metal ions, namely, Sn^{2+}, Cu^{2+}, Pb^{2+}, Cd^{2+}, Mn^{2+}, Zn^{2+}, Fe^{2+}, Co^{2+}, Mg^{2+} and Ni^{2+}. By integrating machine learning algorithms, this approach achieved a remarkable validation accuracy of 0.996. When applied to natural water samples, the strategy effectively demonstrated its practical utility for real-world environmental monitoring and metal ion detection.

Owing to their unique electronic and optical properties, metal elements are indispensable in industrial applications. For instance, diverse metal ions coordinate with ligands to construct functional materials with catalytic[1,2] or magnetic[3,4] properties. Beyond these technological uses, metals play critical roles in environmental homeostasis. Essential ions such as Mg^{2+} are vital for photosynthesis[5] and carbon cycling[6] to sustain ecological balance. Other key ions, including Fe^{2+}, Zn^{2+} and Cu^{2+}, serve as critical cofactors in metalloenzymes, driving fundamental biological processes such as oxygen transport[7], electron transfer[8] and nucleic acid synthesis[9,10]. Conversely, heavy metal ions pose critical risks: even at trace concentrations, they can disrupt aquatic ecosystems and accumulate in food chains, threatening biodiversity and human health[11]. Consequently, monitoring the concentration and speciation of metal ions is essential to safeguard ecological equilibria and public well-being.

Established methods for metal ion detection, such as atomic absorption spectroscopy (AAS), inductively coupled plasma mass spectrometry (ICP-MS) and electrochemical approaches, each exhibit distinct advantages and limitations. As a cornerstone technique, AAS is widely employed for elemental composition analysis but is largely restricted to single-element detection[12]. ICP-MS offers exceptional sensitivity with low detection limits and multi-element capability, yet it demands high costs and specialized operational expertise[13]. Electrochemical methods, including voltammetry, provide portability but suffer from critical drawbacks, such as poor reproducibility, limited long-term stability and frequent electrode fouling issues[14,15]. While these techniques are foundational in analytical chemistry, they commonly rely on bulky instrumentation, require sophisticated operation and struggle to balance sensitivity with portability. Consequently, there remains an urgent need to develop a portable, rapid and cost-effective strategy that can address these challenges, one that integrates high sensitivity, ease of use and field-deployable functionality for efficient metal ion detection.

As an emerging single-molecule sensor, nanopores are widely applied to characterize amino acids[16,17], nucleic acids[18] and

[1]State Key Laboratory of Analytical Chemistry for Life Sciences, School of Chemistry and Chemical Engineering, Nanjing University, Nanjing, China. [2]Chemistry and Biomedicine Innovation Center (ChemBIC), ChemBioMed Interdisciplinary Research Center, Nanjing University, Nanjing, China. e-mail: shuo.huang@nju.edu.cn

https://doi.org/10.1038/s44221-025-00544-2

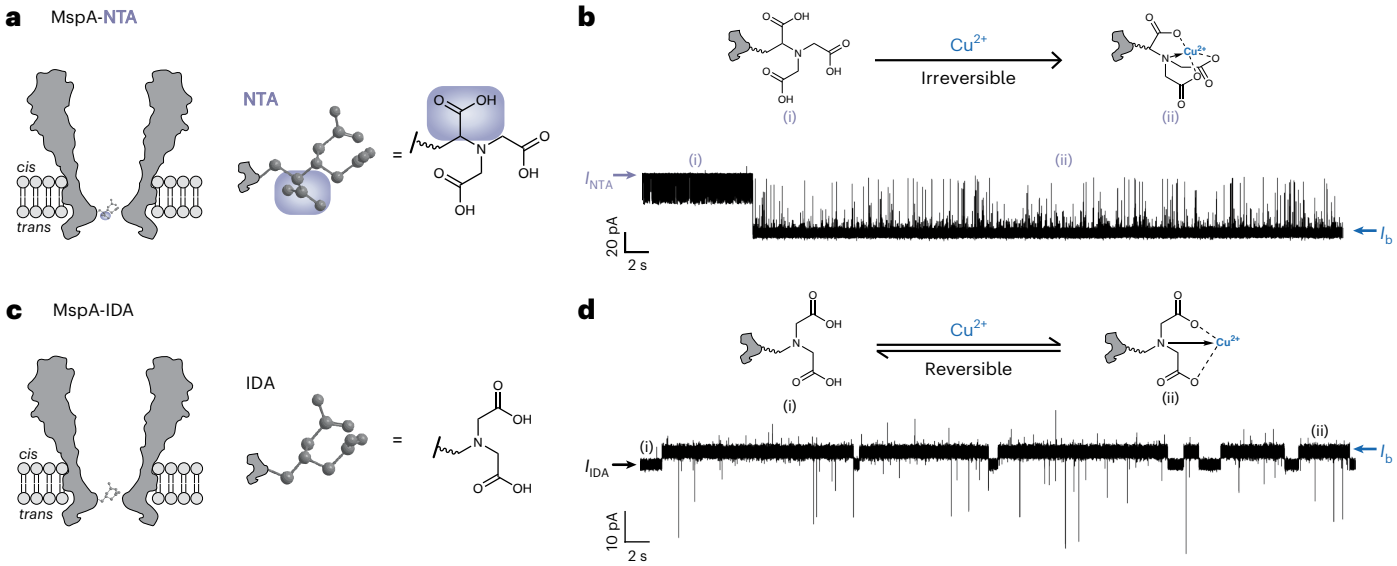

Fig. 1 | Nanopore engineering for divalent metal ion analysis. a,**c**, Schematic diagrams of MspA-NTA (**a**) and MspA-IDA (**c**). Compared with IDA, the NTA adapter contains an additional carboxymethyl group (violet region). **b**,**d**, Representative current versus time traces of Cu^{2+} sensing with MspA-NTA (**b**) and MspA-IDA (**d**). For MspA-NTA, Cu^{2+} binding induced an abrupt and irreversible decrease in the current. Here, I_{NTA} denotes the open-pore current of MspA-NTA (i, violet arrow) and I_b represents the Cu^{2+}-induced blockage current (ii, blue arrow). In contrast, MspA-IDA sensing showed repetitive transitions between the open-pore current of MspA-IDA (I_{IDA}, i, black arrow) and the Cu^{2+}-induced blockage current (I_b, ii, blue arrow). Measurements were performed as described in the Methods using a buffer of 1.5 M KCl and 100 mM MOPS (pH 7.0). A continuous transmembrane potential of +80 mV was applied. Cu^{2+}, treated as a model analyte, was added to the *trans* chamber to a final concentration of 4 μM.

saccharides[19]. For metal ion sensing, this can be achieved by engineering metal-ion binding sites within the nanopore lumen[20,21] or by monitoring differences in probe molecule translocation kinetics in the presence or absence of metal ions[22–26]. However, current research in this field is limited by two key challenges: the range of detectable metal ions using the same technique remains narrow and studies rarely extend to the analysis of heterogeneous samples, such as natural water samples. *Mycobacterium smegmatis* porin A (MspA), a conical biological nanopore[27], has primarily been used for nucleic acid[28] and peptide sequencing[29,30]. With suitable adapters, it has previously been shown to identify ions[31–33] and small molecules[34,35]. Although its high-resolution sensing of small molecules has suggested its potential to simultaneously identify a large variety of metal ions, the simultaneous identification of common metal ions, including Sn^{2+}, Cu^{2+}, Pb^{2+}, Cd^{2+}, Mn^{2+}, Zn^{2+}, Fe^{2+}, Co^{2+}, Mg^{2+} and Ni^{2+}, by a nanopore in the same assay has never been achieved.

Screening of nanopore adapters for divalent metal ion analysis

In principle, the covalent attachment of a ligand to a nanopore constriction enables the engineered nanopore to detect any metal ion that binds to the introduced ligand. However, the direct and unambiguous identification of diverse metal ions from natural water samples requires the optimization of both the pore resolution and ligand binding strength. In our previous work, we conjugated nitrilotriacetic acid (NTA), a tetradentate ligand bearing three carboxymethyl groups branching out from a central nitrogen atom (Fig. 1a), to MspA to generate MspA-NTA. This modification induced the irreversible binding of metal ions such as Ni^{2+} and Cu^{2+} (ref. 36). While this irreversible chelation strategy has endowed nanopores with sensing capabilities for amino acids[34], the B vitamins[37] and thyroid hormones[36], it has proved unsuitable for direct metal ion detection. As demonstrated with Cu^{2+} as a model analyte (Fig. 1b), irreversible binding hinders dynamic sensing. Although MspA-NTA has previously been used to sense rare earth metals, this required a secondary mobile adapter, an approach deemed experimentally cumbersome. Moreover, the dual-ligand strategy is ineffective for metal ions commonly found in natural water, such as Cu^{2+}, Mn^{2+} and Zn^{2+} (ref. 33).

To achieve reversible metal ion binding, we used iminodiacetic acid (IDA), a simplified tridentate ligand lacking one carboxymethyl group compared with NTA (Fig. 1c). For simplicity, the IDA-appended nanopore is referred to as MspA-IDA. Using MspA-IDA to sense Cu^{2+} revealed repetitive current transitions between the open-pore current (I_{IDA}) and blockage current (I_b; Fig. 1d). These measurements, conducted under identical conditions to those for MspA-NTA (Fig. 1b,d), confirmed that IDA is more suitable for direct metal ion sensing. The results further suggest that MspA-IDA has broad potential for detecting diverse metal ions. Details of the preparation of MspA-NTA and MspA-IDA are provided in the Methods, genes encoding MspA monomers are summarized in Supplementary Table 1 and MspA-IDA conductance data are presented in Supplementary Table 2 and Supplementary Fig. 1.

Nanopore identification of various divalent metal ions using MspA-IDA

The sensing of diverse divalent metal ions (M^{2+}) using MspA-IDA was subsequently explored (Fig. 2a). The IDA ligand, covalently attached to the nanopore constriction, coordinates with various M^{2+} ions, generating unique current signatures that can be used for identification (Fig. 2b). We demonstrated the stepwise, single-molecule construction of MspA-IDA via single-channel recording. Initially, the insertion of $(N90C)_1(M2)_7$ (ref. 38), the unmodified MspA hetero-octamer (Supplementary Fig. 1 and Methods), into the lipid bilayer yielded an open-pore current (I_o, Fig. 2c(i)). Upon adding IDA maleimide, an abrupt drop in current to I_{IDA} (~130 pA) was observed, indicating successful pore functionalization (Fig. 2c(ii)). To validate the M^{2+} sensing capability of the functionalized pore, Mn^{2+} was used as a model analyte. The addition of Mn^{2+} to the *trans* chamber immediately induced reversible current transitions between I_{IDA} and a blocked state (I_b, Fig. 2c(iii)), confirming the specific binding of the ion.

Control experiments with unmodified MspA hetero-octamer ($(N90C)_1(M2)_7$) or MspA homo-octamer (M2 MspA) showed no binding events, highlighting the essential role of the IDA ligand (Supplementary Fig. 2). To identify suitable M^{2+} for MspA-IDA sensing, a

https://doi.org/10.1038/s44221-025-00544-2

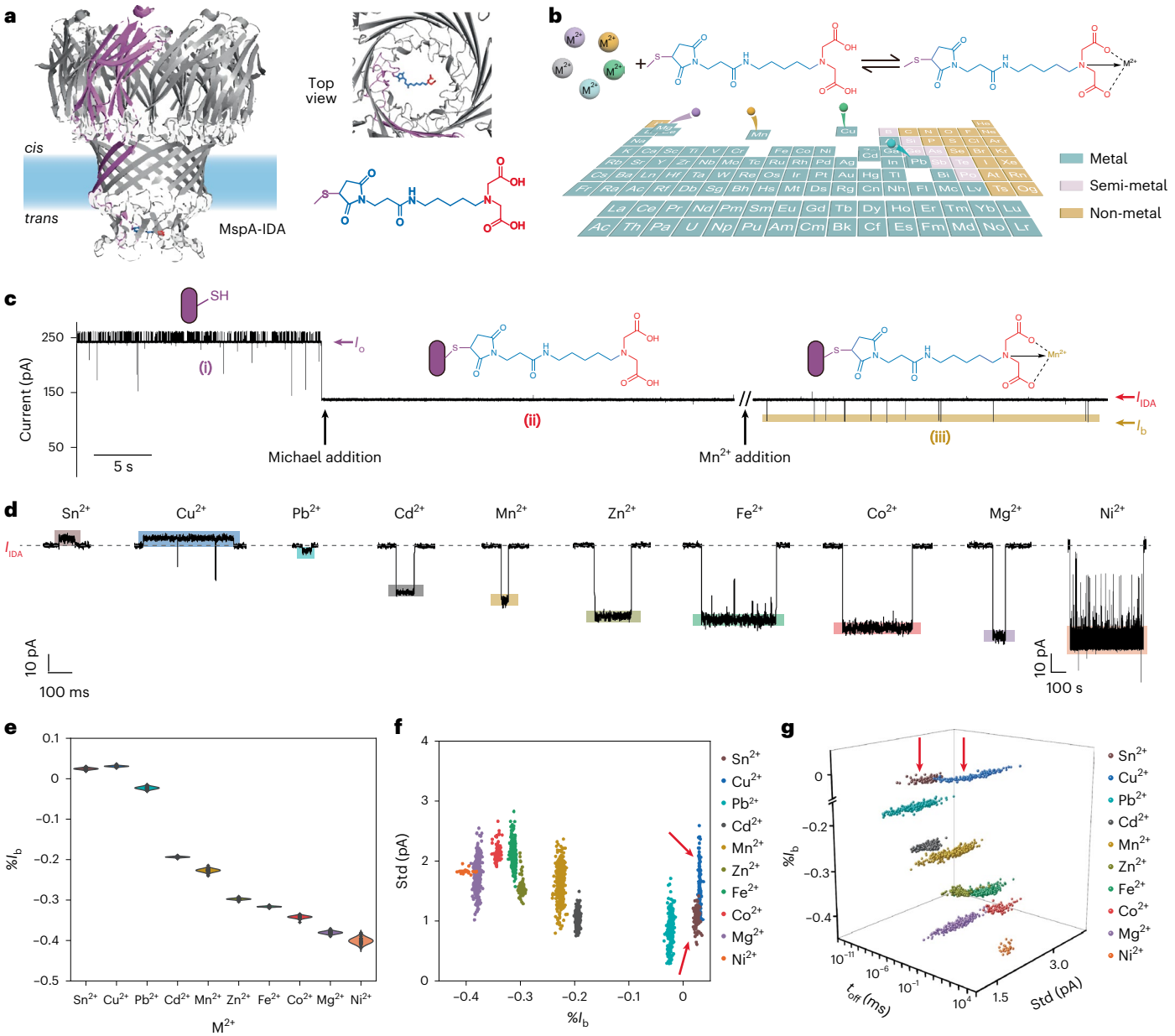

Fig. 2 | Nanopore identification of M^{2+} using MspA-IDA. a, Structure of MspA-IDA, a hetero-octameric MspA nanopore featuring a single IDA adapter. Inset: top-down view of the MspA-IDA pore architecture. **b**, Mechanistic illustration of nanopore M^{2+} sensing: M^{2+} coordinates with the IDA ligand (red), generating characteristic nanopore binding events that can be used for ion identification. **c**, Single-channel recording of pore modification and metal ion binding. Single-channel recording was conducted using an $(N90C)_1(M2)_7$ construct (i). Covalent attachment of the IDA maleimide to the cysteine thiol at position 90 of $(N90C)_1(M2)_7$ yielded MspA-IDA (ii), as evidenced by the abrupt current drop from the open-pore current of $(N90C)_1(M2)_7$ (I_o) to the open-pore current of MspA-IDA (I_{IDA}). Subsequent addition of $MnCl_2$ to the *trans* chamber with a final concentration of 2 µM immediately induced highly characteristic binding events, appearing as reversible transitions between I_{IDA} and the blockage current (I_b, iii). Measurements were performed in 1.5 M KCl and 100 mM MOPS (pH 7.0) under a continuous bias of +80 mV. **d**, Representative binding events acquired with different M^{2+} ions. From left to right: representative events of Sn^{2+}, Cu^{2+}, Pb^{2+}, Cd^{2+}, Mn^{2+}, Zn^{2+}, Fe^{2+}, Co^{2+}, Mg^{2+} and Ni^{2+}. **e**, Violin plot of $\%I_b$ values for different M^{2+} binding events. Statistical analysis (n = 930 events) showed effective discrimination of metal ions based solely on $\%I_b$. The width of the horizontal shaded area represents the probability density of the data distribution at each value. Each vertical diamond pattern represents an individual data point. **f**, A 2D event scatter plot of $\%I_b$ versus Std for ten M^{2+} (n = 2,816 events). The event clusters of Sn^{2+} and Cu^{2+} show overlaps (indicated by red arrows). **g**, A 3D event scatter plot of $\%I_b$, Std and t_{off} for ten M^{2+}. A new parameter, t_{off}, is incorporated, with which all ten M^{2+} are completely distinguishable. In total, 2,816 events were included to generate the statistics.

screening assay was performed (Supplementary Fig. 3). Briefly, no signals were obtained for Ca^{2+}, Sr^{2+}, Pd^{2+}, Ba^{2+} or Pt^{2+} (Supplementary Fig. 4); however, successful sensing of Sn^{2+}, Cu^{2+}, Pb^{2+}, Cd^{2+}, Mn^{2+}, Zn^{2+}, Fe^{2+}, Co^{2+}, Mg^{2+} and Ni^{2+} was observed, demonstrating the generality of MspA-IDA for sensing (Fig. 2d).

Similar measurements were performed with MspA-NTA, with Fe^{2+}, Co^{2+}, Ni^{2+} and Cu^{2+} all binding irreversibly to the NTA ligand (Supplementary Fig. 5). When Mg^{2+} and Sn^{2+} were analysed using MspA-NTA, reproducible events were observed (Supplementary Fig. 6), indicating that both metal ions interact reversibly with the NTA ligand under these conditions. In contrast, measurements of MspA-NTA with Mn^{2+}, Zn^{2+}, Cd^{2+} and Pb^{2+} yielded no detectable signals, demonstrating weak interactions between these metal ions and the NTA ligand under the measurement conditions (Supplementary Fig. 7). These findings

https://doi.org/10.1038/s44221-025-00544-2

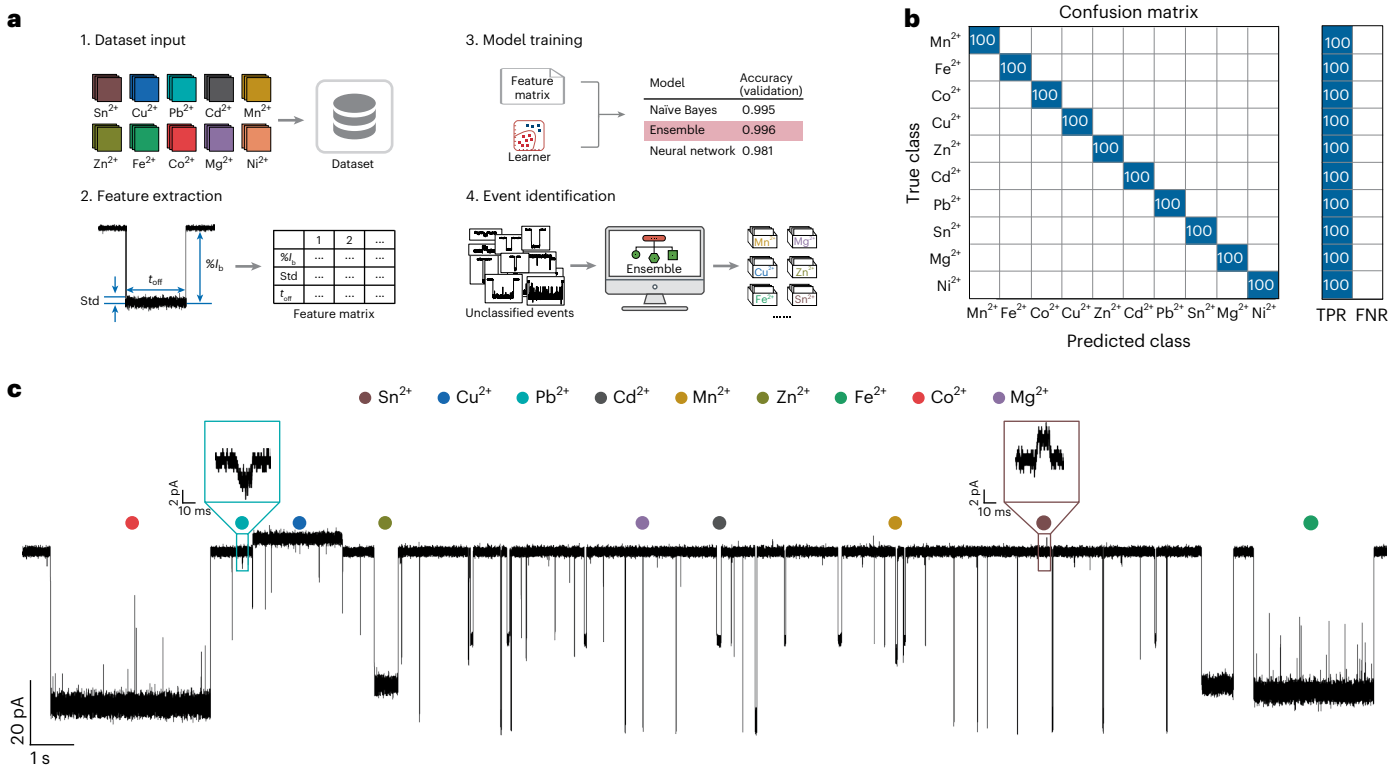

Fig. 3 | Machine learning-based identification of M^{2+} ions. a, Workflow for machine learning classification. Each M^{2+} class contained 100 events, except Ni^{2+}, which contained 30 events. Three event features, $\%I_b$, Std and t_{off}, were extracted to construct a feature matrix. Classification models were trained using MATLAB's Classification Learner toolbox, with the performance evaluated via tenfold cross-validation. The ensemble model achieved the highest validation accuracy (0.996). **b**, Confusion matrix for the testing set using the ensemble model. True positive rates (TPR) and false negative rates (FNR) for each ion class are displayed on the right. **c**, Representative current versus time traces acquired during the simultaneous sensing of nine M^{2+}. The events are shown in more detail in Supplementary Fig. 29. Metal ion salts, including acetates for Pb^{2+} and Sn^{2+} and chlorides for the other M^{2+}, were simultaneously added to the *trans* chamber to give the following final concentrations: 1 μM Pb^{2+}, 2 μM Co^{2+}, 4 μM Zn^{2+}, 5 μM Mn^{2+}, Fe^{2+} and Cu^{2+}, 10 μM Cd^{2+}, 200 μM Mg^{2+} and 250 μM Sn^{2+}. A continuous bias of +80 mV was applied. Events were predicted using the trained ensemble model and are labelled for each ion accordingly.

thus underscore the broader binding versatility of MspA-IDA for M^{2+} compared with MspA-NTA.

Event features were systematically characterized, including inter-event duration (t_{on}), dwell time (t_{off}), percentage blockage ($\%I_b = (I_b - I_{IDA})/I_{IDA}$) and current trace standard deviation (Std), as detailed in Supplementary Fig. 8. The corresponding data for all M^{2+} are presented in Supplementary Table 3. During M^{2+} sensing, within a specific range of M^{2+} concentrations, the event count for a specific M^{2+} per minute (F) exhibits a linear correlation with the concentration of the ion (Supplementary Figs. 9–18 and Supplementary Tables 4 and 5). Quantitative analyses of the event features for all metal ions are provided in Supplementary Figs. 19 and 20. Notably, Cu^{2+} and Sn^{2+} induced positive-going events ($I_b > I_{IDA}$, Supplementary Fig. 21), whereas all other M^{2+} ions produced negative-going events ($I_b < I_{IDA}$, Supplementary Fig. 21), showcasing distinct sensing behaviours critical for ion discrimination. Unlike nanopore blockage caused by the translocation of macromolecules, metal ions are considerably smaller in size. Thus, the shape and polarity of nanopore events induced by metal ion binding may arise from multiple factors beyond just the size of the analyte. When captured by the IDA ligand, certain M^{2+} might simultaneously coordinate with neighbouring amino acid residues within the pore lumen. The resulting configuration may in turn generate a more open pore constriction, thereby producing positive-going events for certain types of M^{2+}.

To mitigate interference from noise events, the density-based spatial clustering of applications with noise (DBSCAN) algorithm was employed to filter out events that do not form distinct clusters (Supplementary Figs. 22–26). The conical lumen of MspA provides high-resolution discrimination, enabling most M^{2+} ions to be identified solely by their percentage blockage ($\%I_b$; Fig. 2e). Notably, Ni^{2+} exhibits exceptionally long event durations, ranging from minutes to hours (Supplementary Fig. 27), complicating collection within standard measurement periods and limiting the number of Ni^{2+} events in the statistical dataset. Despite this, the uniquely prolonged dwell time of Ni^{2+} events also allows for unambiguous identification. In the two-dimensional (2D) scatter plot of $\%I_b$ and Std for the ten M^{2+} ions (Fig. 2f), partial overlap is observed between the event populations of Sn^{2+} and Cu^{2+}. However, incorporating a third parameter, event dwell time (t_{off}), into a three-dimensional (3D) scatter plot of $\%I_b$, Std and t_{off} enabled clear discrimination of all ten ions (Fig. 2g). This demonstrates the advantage of multi-feature analysis for unambiguous metal ion discrimination, surpassing single parameter approaches. In this Article, as summarized in Supplementary Table 6, the limit of detection (LOD) is defined as the minimum concentration of M^{2+} required to detect a minimum of two binding events during 10 min of continuous measurement.

So far, we have demonstrated simultaneous nanopore sensing of ten common M^{2+} under identical conditions, the largest such collection reported for a single nanopore measurement, excluding previous rare earth element studies[33]. However, the nanopore rare earth element sensor requires a secondary mobile ligand, which complicates the process, and was found to be unsuitable for metal ions such as Zn^{2+}, Cu^{2+}, Co^{2+} and Mn^{2+}, which pose urgent challenges for environmental sensing applications. Notably, this is the first report of the nanopore sensing of Sn^{2+} and Mg^{2+}, expanding the applicability of the technique to previously uncharacterized ions.

https://doi.org/10.1038/s44221-025-00544-2

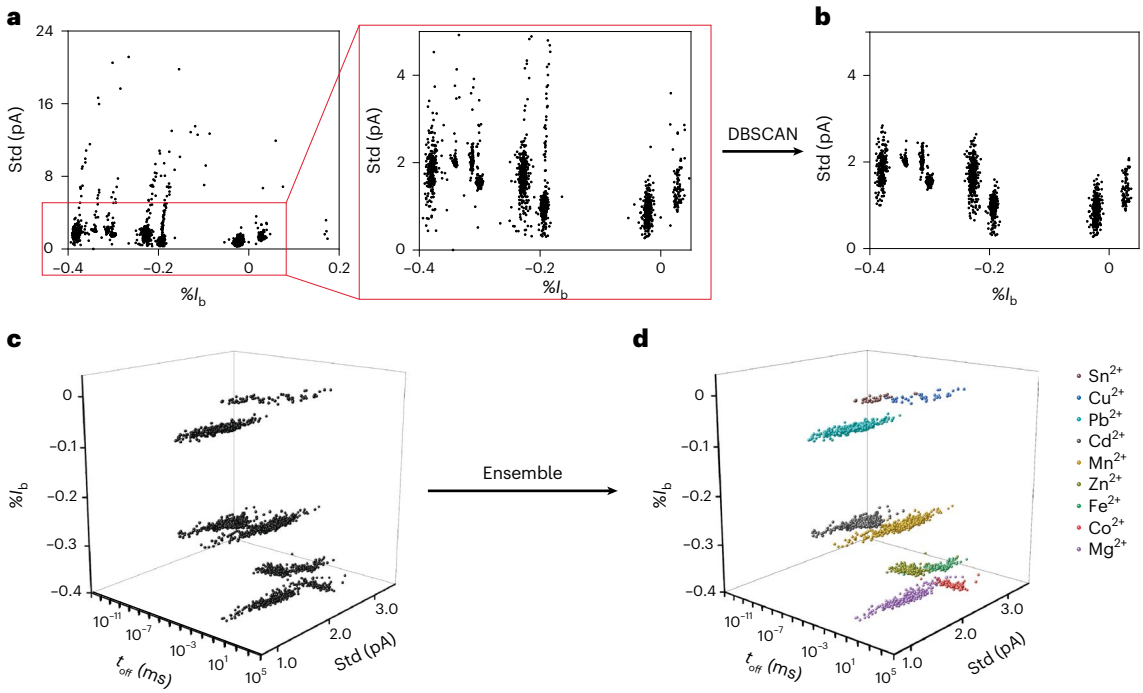

Fig. 4 | Machine learning-assisted event identification. a, The original 2D event scatter plot of %I_b versus Std derived from the raw data acquired during simultaneous sensing of nine M^{2+} (n = 2,480). **b**, The 2D scatter plot of %I_b versus Std after cluster analysis treatment using DBSCAN (n = 2,278). **c**, The 3D event scatter plot of %I_b, Std and t_{off} after cluster analysis using DBSCAN (n = 2,278). **d**, The corresponding 3D event scatter plot of %I_b, Std and t_{off} with machine learning-predicted labels. Machine learning automatically predicted the ion identities, with events colour-coded by the corresponding M^{2+} classes. The distribution of each M^{2+} type is consistent with those acquired separately (Fig. 2g).

Identification of M^{2+} by machine learning

To mitigate human bias and enable automated data analysis, machine learning was implemented using the results reported above (see Methods for details). The events of different M^{2+} classes were randomly selected to construct the dataset, with each class containing 100 events, except Ni^{2+}, which included 30 events due to limited data collection efficiency. The dataset was partitioned into an 80% training subset and a 20% testing subset for model training and evaluation. Three event features, %I_b, Std and t_{off}, were automatically extracted to build the feature matrix. Using MATLAB's Classification Learner toolbox (https://www.mathworks.com/help/stats/classificationlearner-app.html), we trained three algorithms, naïve Bayes, ensemble and neural network, using ten-fold cross-validation for performance assessment. The ensemble model achieved the highest validation accuracy (0.996) and a perfect testing accuracy (1.000), as detailed in Supplementary Table 7. This trained ensemble model was subsequently used to predict unlabelled events (Fig. 3a). The confusion matrix for the testing set (Fig. 3b) showed 100% accuracy across all classes, underscoring the high-quality discriminative power of the dataset. To further validate model robustness, a learning curve analysis was performed (Supplementary Fig. 28). The results indicated that when the size of the training set exceeded 363 events, the validation accuracy stabilized at 0.993, demonstrating consistent performance with increased data volume. A representative current trace acquired during simultaneous sensing of these M^{2+} ions is shown in Fig. 3c. Notably, Ni^{2+} was excluded due to its prolonged event duration, which complicates data collection. Considering the varying capture rates of different M^{2+} (Supplementary Table 8), the concentrations of different M^{2+} were adjusted during mixed-sensing experiments to achieve a balanced event occurrence rate. For the measurements, metal ion salts, including acetates for Pb^{2+} and Sn^{2+} and chlorides for the other M^{2+} ions, were simultaneously added to the *trans* chamber to give the following final concentrations: 1 μM Pb^{2+}, 2 μM Co^{2+}, 4 μM Zn^{2+}, 5 μM Mn^{2+}, Fe^{2+} and Cu^{2+}, 10 μM Cd^{2+}, 200 μM Mg^{2+} and 250 μM Sn^{2+}. Each event was subsequently predicted by the pre-trained ensemble model and labelled accordingly (Fig. 3c and Supplementary Fig. 29).

Event features were automatically extracted to generate scatter plots, with background noise events removed via DBSCAN (Fig. 4a,b). Using the trained model, unlabelled events were classified automatically. In the derived 3D scatter plot of %I_b, Std and t_{off} (Fig. 4c,d), event distributions exactly matched those observed in Fig. 2g, confirming consistent discriminative patterns across datasets. These results demonstrate the successful construction of a fully automated classifier to identify diverse M^{2+} as a mixture.

Nanopore analysis of M^{2+} in natural water samples

Appropriate concentrations of essential M^{2+} in aquatic ecosystems play critical roles in biological metabolism[39], whereas excessive heavy metal ions induce toxicity and disrupt ecological balance[40]. Thus, monitoring their concentrations in water bodies is vital to maintain ecosystem equilibrium and organismal health[41]. The machine learning-integrated method presented here offers exceptional sensitivity and automated recognition capabilities, providing a robust tool for sustainable water resource management, pollution control and ecological protection.

To test the anti-interference capability of this method against natural water sample matrices, small molecules and macromolecules that may exist in water samples, including glucose, glycine, humic acid and single-stranded DNA, were used as representative interferents. No corresponding events were detected with MspA-IDA (Supplementary Figs. 30 and 31), confirming the specificity of MspA-IDA for M^{2+} and validating its anti-interference capability. Six natural water samples from different geographical locations, namely, tap water, pond water, lake water, river water, seawater and salt lake water, were collected for nanopore measurements (Extended Data Fig. 1 and Methods). These samples were selected due to their accessibility and importance in aquatic systems, allowing the performance of this

https://doi.org/10.1038/s44221-025-00544-2

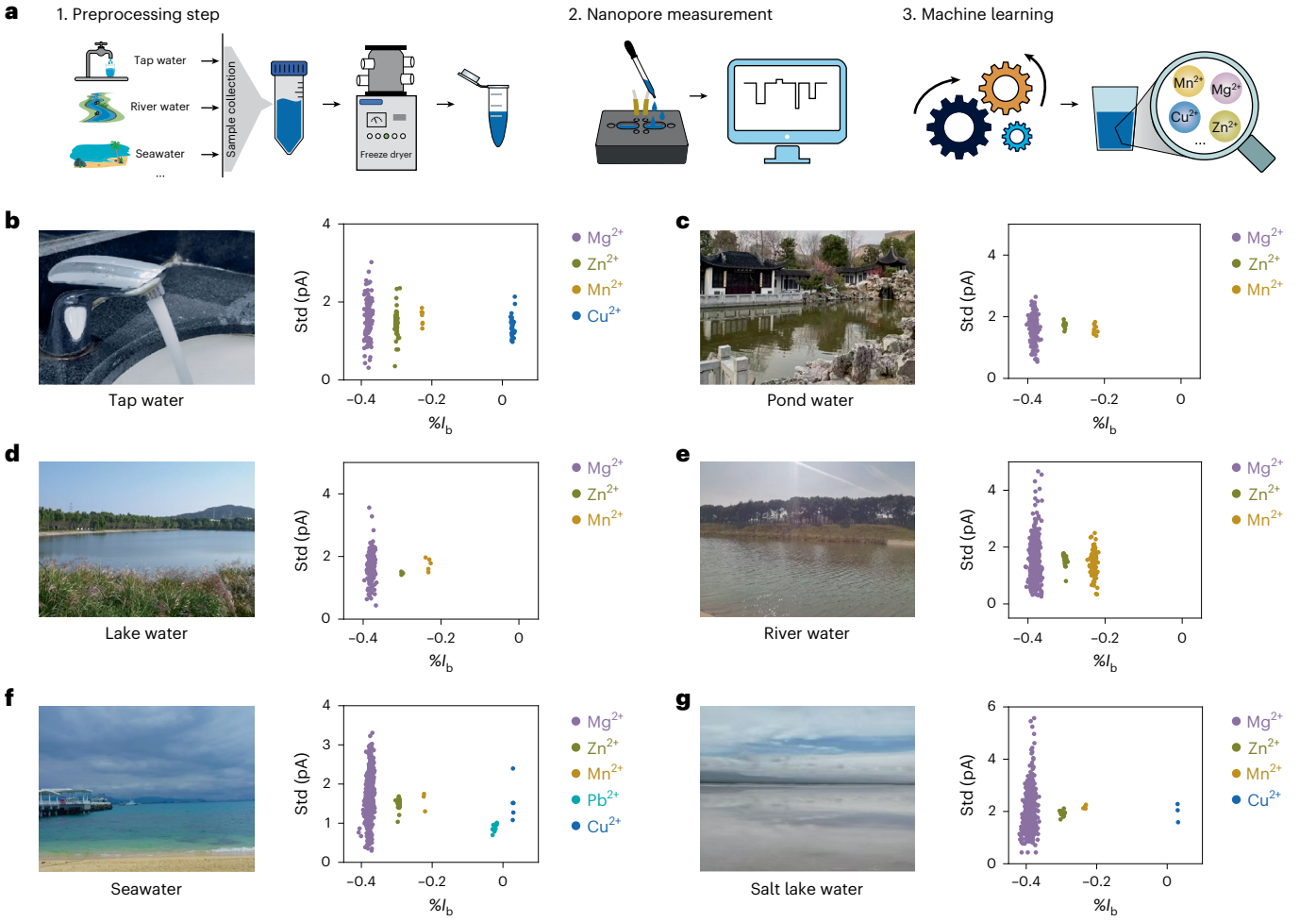

i

Sample	Mg^{2+} (mg l^{-1})	Zn^{2+} (mg l^{-1})	Mn^{2+} (mg l^{-1})	Cu^{2+} (mg l^{-1})	Pb^{2+} (mg l^{-1})
Tap water	11.8 ± 1.0	0.35 ± 0.06	0.0304 ± 0.0017	0.20 ± 0.09	–
Pond water	15.5 ± 0.8	0.01 ± 0.01	0.040 ± 0.004	–	–
Lake water	17.2 ± 0.6	0.0078 ± 0.0011	0.026 ± 0.004	–	–
River water	18.7 ± 1.6	0.056 ± 0.017	0.09 ± 0.03	–	–
Seawater	680 ± 30	1.4 ± 0.5	0.40 ± 0.06	0.5 ± 0.4	2.1 ± 0.2
Salt lake water	(2.0 ± 0.15) × 10^4	4 ± 2	4.2 ± 0.3	3 ± 2	–

Fig. 5 | Nanopore analysis of M^{2+} in natural water samples. a, Workflow for the analysis of natural water samples. Water samples from distinct locations were collected and lyophilized (except for salt lake water) to obtain concentrates. For measurements, concentrates (or undiluted stock solutions for salt lake water) were added to the *trans* chamber (Methods). A continuous bias of +80 mV was applied during the measurements. Events were collected and classified using the pre-trained ensemble model. **b**–**g**, Photographs of the water sources and 2D scatter plots of $\%I_b$ versus Std for tap water (**b**, $n = 653$), pond water (**c**, $n = 235$), lake water (**d**, $n = 344$), river water (**e**, $n = 1{,}512$), seawater (**f**, $n = 1{,}075$) and salt lake water (**g**, $n = 2{,}590$). **h**, Quantitative analysis of M^{2+} in the natural water samples. The data represent the mean ± standard deviation (SD) of three independent measurements ($N = 3$). The error bars denote SD. **i**, Tabulated numerical data of the results shown in **h**.

sensor with environmentally relevant M^{2+} to be evaluated. All samples, except the salt lake water, were further lyophilized and concentrated by different factors to obtain concentrates. To initiate nanopore measurements, 10 µl of tap water, pond water, lake water and river water, 5 µl of seawater and 2 µl of salt lake water (concentrates or salt lake water stock solution) were directly added to the *trans* chamber. All events were then classified using the pre-trained ensemble model (Fig. 5a, Supplementary Fig. 32 and Methods).

Representative current traces acquired with natural water samples are shown in Supplementary Fig. 33. The corresponding 2D scatter plots of $\%I_b$ and Std for the six sample types (Fig. 5b–g and Supplementary Figs. 34–39) reveal that Mg^{2+}, Zn^{2+} and Mn^{2+} were detected across all samples. Cu^{2+} was detected in all samples except river water, pond water and lake water. Its presence in tap water can probably be attributed to copper-based piping, with Cu^{2+} dissolution occurring during water transportation[42]. The river water sampled here

originates from a freshwater resource, where Cu^{2+} concentrations are probably below the detection limit under the measurement conditions. In seawater and salt lake water, the presence of Cu^{2+} or Pb^{2+} may be relevant to anthropogenic activities such as shipping, agriculture and aquaculture[43]. The concentrations of M^{2+} in the natural water samples were also estimated (Fig. 5h,i and Methods). Notably, the failure to detect other M^{2+} in these assays may stem from two scenarios: either they are present in the samples but at concentrations below the assay's LOD or they lack the binding specificity required to interact with the IDA ligand.

To validate the above results, a standard sample containing Zn^{2+}, Mn^{2+} and Cd^{2+} with known concentrations was prepared. Briefly, $ZnCl_2$, $MnCl_2$ and $CdCl_2$ were dissolved simultaneously in 30 ml of ultrapure water, resulting in a final concentration of 0.25 mM for each salt (Methods). For analysis, 10 ml of the above sample was used for ICP-MS measurements, whereas only 6 µl was required for nanopore analysis. As shown in Supplementary Fig. 40, these three M^{2+} ions were successfully detected by both ICP-MS and the nanopore. The quantitative results obtained by the nanopore approach were generally consistent with those from ICP-MS, as well as with the true concentrations of the standard sample, confirming the validity of this nanopore technique. In addition, the seawater sample was analysed quantitatively by ICP-MS. The results were generally consistent with the nanopore method (Supplementary Fig. 41), demonstrating that this nanopore technique is suitable for the quantitative analysis of M^{2+} in natural water samples. Therefore, by integrating both the qualitative identification and quantitative estimation capabilities, this method demonstrates substantial potential for environmental M^{2+} detection, enabling early risk assessment and supporting sustainable environmental management.

To explore the suitability of the technique for portable natural water analysis, all of the above measurements were also performed using a portable Orbit mini patch-clamp amplifier (Nanion Technologies; Supplementary Fig. 42). As a representative example, the concentrated seawater sample described in the Methods was used. For measurements, 5 µl of the seawater concentrate was added to the microfluidic chip, prompting the immediate emergence of distinct nanopore events. The corresponding 2D scatter plot of $\%I_b$ and Std exhibited a distribution consistent with that shown in Fig. 5, demonstrating that a portable device can effectively analyse water samples. To further confirm the robustness of this method, we conducted measurements to assess the long-term stability (Supplementary Fig. 43) and temperature resistance of the nanopore (Supplementary Fig. 44). The results demonstrate that nanopore sensing can be performed continuously for hours and over a temperature range of 0 to 50 °C, confirming the suitability of the method for on-site detection, an essential feature for real-world environmental monitoring. Compared with established methods for M^{2+} analysis, this nanopore technique holds distinct advantages in portability and cost. It offers the potential for miniaturized, field-deployable devices and notably lower operational expenses. In terms of robustness, the nanopore approach demonstrates superior performance over voltammetry, exhibiting enhanced signal reproducibility, stronger resistance to matrix interference and improved performance under extreme conditions. However, its current form still shows a lower throughput and an unsatisfactory LOD compared with ICP-MS.

Conclusion

By chemically conjugating an IDA ligand to a hetero-octameric MspA (MspA-IDA), an engineered MspA nanopore with M^{2+} sensing capability has been developed. Under identical conditions, a total of ten common M^{2+}, namely, Sn^{2+}, Cu^{2+}, Pb^{2+}, Cd^{2+}, Mn^{2+}, Zn^{2+}, Fe^{2+}, Co^{2+}, Mg^{2+} and Ni^{2+}, could be simultaneously detected. By analysing the characteristics of the generated events, all ten metal ions could be discriminated from each other. When integrated with machine learning, a remarkable validation accuracy of 0.996 was achieved, underscoring the exceptional resolution and reliability of the strategy. This sensing approach was further validated through analysis of six natural water samples, namely, tap water, pond water, lake water, river water, seawater and salt lake water. Qualitative and quantitative profiling of the major M^{2+} ions in these natural water samples was achieved, demonstrating its practical utility in real-world environmental analysis. Compared with existing nanopore-based methods, the strategy presented here offers distinct advantages: it is simpler and provides higher-quality data with minimal sample preprocessing. Notably, this research encompasses a wide array of M^{2+}, many of which are critical to daily life and human health, expanding its relevance to diverse environmental and health monitoring contexts. When paired with portable instrumentation, the method holds considerable promise for on-site, real-time metal ion detection, an attribute highly desirable for field applications. In the future, to increase the number of detectable metal ion types, a further optimized ligand compatible with more metal ion types may be developed or a multifunctional array of multiple types of nanopore may be applied. Overall, these findings establish the developed nanopore metal ion sensor as a vital tool to advance environmental monitoring, support sustainable resource management and address emerging challenges in pollution control.

Methods

Nanopore preparation

All core measurements in this work were performed with MspA-IDA, which is an IDA-appended hetero-octameric MspA. This hetero-octameric MspA was prepared similarly to a previous report[38]. Briefly, two genes respectively coding for M2 MspA-D16H6 and N90C MspA-H6 (Supplementary Table 1) were simultaneously inserted into a pET-30a(+) plasmid and expressed with *Escherichia coli* BL21(DE3) pLysS competent cells (GenScript). A hexahistidine tag (H6) was added to the carboxy terminus of both genes to assist purification by nickel affinity chromatography. A 16 aspartic acid tag (D16) was added to the end of the M2 MspA-D16H6 gene to enhance discrimination between different assembly types of M2 MspA-D16H6 and N90C MspA-H6 during gel electrophoresis. The target hetero-octameric MspA assembly, which contains a single unit of N90C MspA-H6 and seven units of M2 MspA-D16H6, was collected during purification. For simplicity, this hetero-octameric MspA assembly is referred to as $(N90C)_1(M2)_7$.

Experimentally, *E. coli* BL21(DE3) pLysS containing the recombinant plasmid was spread onto an Luria–Bertani (LB) agar plate supplemented with 50 µg ml^{-1} ampicillin and 34 µg ml^{-1} chloramphenicol. Following incubation at 37 °C for 15 h, a single colony was selected and inoculated into LB broth containing the same antibiotics (50 µg ml^{-1} ampicillin and 34 µg ml^{-1} chloramphenicol). The culture was incubated overnight at 37 °C with shaking at 3 *g* until the optical density at 600 nm reached 0.7. Protein expression was induced by adding isopropyl-β-D-thiogalactoside to a final concentration of 0.1 mM. The induced culture was then shaken at 16 °C and 3 *g* for 24 h. Finally, bacterial cells were collected by centrifuging at 1,500 *g* for 20 min at 4 °C, yielding a pellet for subsequent treatment.

The bacterial pellet was resuspended in 150 ml lysis buffer (100 mM Na_2HPO_4/NaH_2PO_4, 0.1 mM EDTA, 150 mM NaCl and 0.5% (w/v) Genapol X-80, pH 6.5) and incubated at 60 °C for 50 min. The suspension was then centrifuged at 16,000 *g* for 40 min at 4 °C and the supernatant was collected. Nickel affinity chromatography was used for purification, with the sample eluted using a linear imidazole gradient generated by mixing buffer A (0.5 M NaCl, 20 mM HEPES, 5 mM imidazole, 2 mM TCEP and 0.5% (w/v) Genapol X-80, pH 8.0) and buffer B (0.5 M NaCl, 20 mM HEPES, 500 mM imidazole, 2 mM TCEP and 0.5% (w/v) Genapol X-80, pH 8.0). Eluted fractions were collected and analysed by 4–15% SDS–PAGE. Further separation of hetero-octameric MspAs was performed using 10% SDS–PAGE with a tris-glycine buffer system. Following staining with Coomassie brilliant blue, the gel regions containing the target hetero-octameric MspA assembly were excised and immersed in de-staining solution (150 mM NaCl, 15 mM Tris-HCl, 0.2% n-dodecyl-β-D-maltoside (DDM), 0.5% Genapol X-80, 5 mM TCEP

and 10 mM EDTA, pH 7.5) for 12 h. The target protein $(N90C)_1(M2)_7$ was recovered and stored at −80 °C for subsequent use.

Preparation of $(N90C)_1(M2)_7$ modified with different adapters

To conjugate $(N90C)_1(M2)_7$ to NTA, 1 µl $(N90C)_1(M2)_7$ was mixed with 8 µl *N*-[5-(3′-maleimidopropylamido)-1-carboxypentyl]iminodiacetic acid (maleimido-C3-NTA) (20 mM, dissolved in 1.5 M KCl buffer) at room temperature for 4 h. The resulting product, referred to as MspA-NTA, was used immediately or stored at −80 °C for long-term preservation.

For the conjugation of IDA, 0.4 µl of pre-prepared $(N90C)_1(M2)_7$, 0.6 µl of IDA maleimide (20 mM, dissolved in 1.5 M KCl buffer) and 4 µl of 1.5 M KCl buffer (1.5 M KCl and 100 mM MOPS, pH 7.0) were mixed at room temperature for 10 min. The IDA-modified MspA nanopore, denoted MspA-IDA for simplicity, was subsequently stored at −80 °C for long-term use.

Nanopore measurements

All nanopore measurements were performed as described previously[33]. Briefly, the measurement device consisted of two chambers separated by a Teflon film containing a 100-µm aperture. Before measurements, the aperture was treated with a 2% (v/v) hexadecane solution in pentane. The electrically grounded *cis* chamber and the opposing *trans* chamber were each filled with 500 µl of 1.5 M KCl buffer (1.5 M KCl and 100 mM MOPS, pH 7.0). Ag/AgCl electrodes were immersed in both chambers to establish electrical contact between the buffers and the patch-clamp amplifier. A 100 µl pentane solution of 1,2-diphytanoyl-*sn*-glycero-3-phosphocholine (5 mg ml^{-1}) was added to both chambers for lipid bilayer formation. MspA-IDA was introduced into the *cis* chamber to initiate pore insertion. Following single nanopore insertion, excess nanopores were removed by exchanging the buffer in the *cis* chamber.

Single-channel recordings were acquired using an Axopatch 200B patch-clamp amplifier coupled with a Digidata 1550B digitizer. Signals were sampled at 25 kHz and low-pass filtered at a corner frequency of 1 kHz. Unless specified otherwise, all measurements were performed in a 1.5 M KCl buffer solution (1.5 M KCl and 100 mM MOPS, pH 7.0) at an applied voltage of +80 mV. Analytes were added to the *trans* chamber at the desired final concentration.

Data analysis

Nanopore events were identified using the 'single-channel search' function in Clampfit 10.7. Axon ABF files were first imported into MATLAB via the 'abfload' function (downloaded from https://www.mathworks.com/matlabcentral/fileexchange/6190-abfload). Event features, including $\%I_b$, Std and t_{off}, were extracted using a custom algorithm in MATLAB. Scatter plots, histograms, violin plots and curve fittings were generated in Origin 9.2 (Origin Lab) and GraphPad Prism 9.

Machine learning analyses were conducted using MATLAB. Each analyte class comprised 100 events, except for Ni^{2+}, which included 30 events. The dataset was divided into an 80% training set and a 20% testing set. Features, including $\%I_b$, Std and t_{off}, were extracted to construct a feature matrix. The training set was input into MATLAB's Classification Learner toolbox for model training. Six algorithms, namely, support vector machine, *k*-nearest neighbours, ensemble, naïve Bayes, neural network and discriminant analysis, were selected and evaluated. Based on tenfold cross-validation results and testing accuracy, the ensemble model was found to exhibit optimal performance. A confusion matrix generated from the training set was used to assess model performance. The trained model was subsequently applied to classify unknown events.

Sampling sites, times and depths

Tap water, pond water, lake water and river water samples were collected in Nanjing, China, on 10 March 2024. Seawater was sampled from Xidao, Sanya, China, on 11 February 2024, while salt lake water was collected from Caka Salt Lake, Qinghai, China, on 4 August 2024. Among these samples, tap water was obtained directly from a faucet in the university laboratory; the other five water types were all collected at a depth of 0.5 m. The sampling locations of all six water samples, including their specific latitude and longitude coordinates, are shown on the map in Extended Data Fig. 1.

Nanopore analysis of natural water samples

Six types of natural water samples, namely, tap water, pond water, lake water, river water, seawater and salt lake water, were processed as described in Supplementary Fig. 32. These samples were subjected to freeze-drying at different concentration ratios: tap water and pond water were concentrated 25- and 30-fold, respectively, while lake water and river water were concentrated 40-fold and seawater was concentrated 5-fold. The resulting concentrates, along with the salt lake water, which was measured directly without freeze-drying, were then analysed using the nanopore approach.

During the experiments, 10 µl of the tap water, pond water, lake water and river water concentrates and 5 µl of the seawater concentrate were each separately added to the *trans* chamber to commence nanopore measurement. For the salt lake water sample, 2 µl of the stock solution was directly added to the *trans* chamber to initiate the measurement.

Nanopore analysis of the standard sample containing three types of metal ion

First, 1.0 mg $ZnCl_2$, 1.4 mg $CdCl_2$ and 0.9 mg $MnCl_2$ were dissolved in 30 ml ultrapure water to a final concentration of 0.25 mM for each salt. To initiate the measurement, 6 µl of the standard sample was added to the *trans* chamber. Nanopore measurements were carried out in a buffer comprising 1.5 M KCl and 100 mM MOPS, pH 7.0, under a continuous bias of +80 mV.

Quantification of metal ions

During the nanopore sensing of natural water samples, events were classified using the trained machine learning algorithm. By defining an experimentally measurable parameter F as the number of events generated by a specific type of metal ion per minute, a variety of metal ion concentration dependence measurements were performed using this nanopore approach (Supplementary Figs. 9–18). According to the experimental results, within a certain range of metal ion concentrations, the value of F is linearly dependent on the concentration of metal ions.

For a specific type of metal ion, the F value can be related to the metal ion concentration (C) as follows:

$$F_i = a_i + b_i C_i \quad (1)$$

where the subscript i (ranging from 1 to 10) corresponds to Mg^{2+}, Zn^{2+}, Mn^{2+}, Cu^{2+}, Pb^{2+}, Fe^{2+}, Ni^{2+}, Sn^{2+}, Cd^{2+} and Co^{2+}, respectively. The values of a_i and b_i, which are coefficients for specific types of metal ion, were derived from the linear fitting results acquired during the concentration dependence measurements (Supplementary Table 5 and Supplementary Figs. 9–18).

For the quantitative measurement of specific types of metal ion, using the coefficients a_i and b_i (Supplementary Table 5) and F_i values obtained from the respective measurements, the concentrations of specific types of metal ion can be calculated according to the following equation, derived from equation (1):

$$C_i = \frac{F_i - a_i}{b_i} \quad (2)$$

ICP-MS analysis of the standard sample containing three types of metal ion and the seawater sample

All ICP-MS analyses were conducted using an Agilent 7850 ICP-MS system in 'He' mode. During ICP-MS analysis of the standard sample

containing three types of metal ion, the power of the ICP radio frequency generator was 1,550 W, the sampling depth was 10 mm, the flow rate of the compensation gas was 0.2 l min^{-1}, the atomizing gas flow rate was 1.01 l min^{-1}, the plasma gas flow rate was 15 l min^{-1}, the atomizing chamber temperature was 2 °C, the nebulizer pump speed was 0.1 r.p.s., the extraction lens 1 voltage was 0 V, the extraction lens 2 voltage was −165 V, the omega deflection voltage was −95 V and the lens voltage was 7 V.

During ICP-MS analysis of the seawater sample, the power of the ICP radio frequency generator was 1,550 W, the sampling depth was 10 mm, the flow rate of the compensation gas was 0.25 l min^{-1}, the atomizing gas flow rate was 0.95 l min^{-1}, the plasma gas flow rate was 15 l min^{-1}, the atomizing chamber temperature was 2 °C, the nebulizer pump speed was 0.1 r.p.s., the extraction lens 1 voltage was 0 V, the extraction lens 2 voltage was −145 V, the omega deflection voltage was −80 V and the lens voltage was 10 V.

Reporting summary

Further information on research design is available in the Nature Portfolio Reporting Summary linked to this article.

Data availability

The data supporting the findings of this study are available in the Article and its Supplementary Information. All of the data used to train, evaluate and test the machine learning model are available via Figshare at https://doi.org/10.6084/m9.figshare.30102343.v1 (ref. 44). Source data are provided with this paper.

Code availability

The custom machine learning code is available via Figshare at https://doi.org/10.6084/m9.figshare.30102343.v1 (ref. 44).

References

1. Hill, P. J., Doyle, L. R., Crawford, A. D., Myers, W. K. & Ashley, A. E. Selective catalytic reduction of N_2 to N_2H_4 by a simple Fe complex. *J. Am. Chem. Soc.* **138**, 13521–13524 (2016).
2. Aguado, S., Gómez-Gallego, M., Casarrubios, L. & Sierra, M. A. Electrocatalytic HER performance of [FeFe]-hydrogenase mimics bearing M-salen moieties (M=Zn, Ni, Fe, Mn). *Chem. Eur. J.* **31**, e202403721 (2025).
3. López-Cabrelles, J. et al. Chemical design and magnetic ordering in thin layers of 2D metal–organic frameworks (MOFs). *J. Am. Chem. Soc.* **143**, 18502–18510 (2021).
4. Del Rio, M., Grimalt Escarabajal, J. C., Turnes Palomino, G. & Palomino Cabello, C. Zinc/iron mixed-metal MOF-74 derived magnetic carbon nanorods for the enhanced removal of organic pollutants from water. *Chem. Eng. J.* **428**, 131147 (2023).
5. Farhat, N. et al. Effects of magnesium deficiency on photosynthesis and carbohydrate partitioning. *Acta Physiol. Plant.* **38**, 145 (2016).
6. Isson, T. T. et al. Evolution of the global carbon cycle and climate regulation on Earth. *Global Biogeochem. Cycles* **34**, e2018GB006061 (2020).
7. Jorge, S. E., Ribeiro, D. M., Santos, M. N. N. & de Fátima Sonati, M. in *Sickle Cell Anemia: From Basic Science to Clinical Practice* (eds Costa, F. F. & Conran, N.) 1–22 (Springer, 2016).
8. Kosman, D. J. Multicopper oxidases: a workshop on copper coordination chemistry, electron transfer, and metallophysiology. *J. Biol. Inorg. Chem.* **15**, 15–28 (2009).
9. Fuss, J. O., Tsai, C.-L., Ishida, J. P. & Tainer, J. A. Emerging critical roles of Fe–S clusters in DNA replication and repair. *Biochim. Biophys. Acta Mol. Cell Res.* **1853**, 1253–1271 (2015).
10. Wu, F. U. & Wu, C. W. Zinc in DNA replication and transcription. *Annu. Rev. Nutr.* **7**, 251–272 (1987).
11. Sonone, S., Jadhav, S., Singh Sankhla, M. & Kumar, R. Water contamination by heavy metals and their toxic effect on aquaculture and human health through food chain. *Lett. Appl. NanoBioScience* **10**, 2148–2166 (2020).
12. Djingova, R., Mihaylova, V., Lyubomirova, V. & Tsalev, D. L. Multielement analytical spectroscopy in plant ionomics research. *Appl. Spectrosc. Rev.* **48**, 384–424 (2013).
13. Miller-Ihli, N. J. & Baker, S. A. Trace element composition of municipal waters in the United States: a comparison of ICP-AES and ICP-MS methods. *J. Food Compost. Anal.* **14**, 619–629 (2001).
14. Pujol, L. et al. Electrochemical sensors and devices for heavy metals assay in water: the French groups' contribution. *Front. Chem.* **2**, 19 (2014).
15. Cui, L., Wu, J. & Ju, H. Electrochemical sensing of heavy metal ions with inorganic, organic and bio-materials. *Biosens. Bioelectron.* **63**, 276–286 (2015).
16. Zhang, M. et al. Real-time detection of 20 amino acids and discrimination of pathologically relevant peptides with functionalized nanopore. *Nat. Methods* **21**, 609–618 (2024).
17. Zhang, Y. et al. Peptide sequencing based on host–guest interaction-assisted nanopore sensing. *Nat. Methods* **21**, 102–109 (2023).
18. Sheng, Y., Zhou, K., Liu, Q., Liu, L. & Wu, H.-C. Probing conformational polymorphism of DNA assemblies with nanopores. *Anal. Chem.* **92**, 7485–7492 (2020).
19. Ramsay, W. J. & Bayley, H. Single-molecule determination of the isomers of D-glucose and D-fructose that bind to boronic acids. *Angew. Chem. Int. Ed.* **57**, 2841–2845 (2018).
20. Braha, O. et al. Designed protein pores as components for biosensors. *Chem. Biol.* **4**, 497–505 (1997).
21. Braha, O. et al. Simultaneous stochastic sensing of divalent metal ions. *Nat. Biotechnol.* **18**, 1005–1007 (2000).
22. Tian, Y. et al. A biomimetic mercury(II)-gated single nanochannel. *Chem. Commun.* **49**, 10679–10681 (2013).
23. Chen, L., He, H., Xu, X. & Jin, Y. Single glass nanopore-based regenerable sensing platforms with a non-immobilized polyglutamic acid probe for selective detection of cupric ions. *Anal. Chim. Acta* **889**, 98–105 (2015).
24. Wei, K., Yao, F. & Kang, X.-F. Single-molecule porphyrin-metal ion interaction and sensing application. *Biosens. Bioelectron.* **109**, 272–278 (2018).
25. Wen, S. et al. Highly sensitive and selective DNA-based detection of mercury(II) with α-hemolysin nanopore. *J. Am. Chem. Soc.* **133**, 18312–18317 (2011).
26. Wang, G., Wang, L., Han, Y., Zhou, S. & Guan, X. Nanopore detection of copper ions using a polyhistidine probe. *Biosens. Bioelectron.* **53**, 453–458 (2014).
27. Faller, M., Niederweis, M. & Schulz, G. E. The structure of a mycobacterial outer-membrane channel. *Science* **303**, 1189–1192 (2004).
28. Derrington, I. M. et al. Nanopore DNA sequencing with MspA. *Proc. Natl Acad. Sci. USA* **107**, 16060–16065 (2010).
29. Yan, S. et al. Single molecule ratcheting motion of peptides in a *Mycobacterium smegmatis* porin A (MspA) nanopore. *Nano Lett.* **21**, 6703–6710 (2021).
30. Brinkerhoff, H., Kang, A. S. W., Liu, J., Aksimentiev, A. & Dekker, C. Multiple rereads of single proteins at single–amino acid resolution using nanopores. *Science* **374**, 1509–1513 (2021).
31. Cao, J. et al. Giant single molecule chemistry events observed from a tetrachloroaurate(III) embedded *Mycobacterium smegmatis* porin A nanopore. *Nat. Commun.* **10**, 5668 (2019).
32. Wang, S. et al. Single molecule observation of hard–soft-acid–base (HSAB) interaction in engineered *Mycobacterium smegmatis* porin A (MspA) nanopores. *Chem. Sci.* **11**, 879–887 (2020).

33. Sun, W. et al. Nanopore discrimination of rare earth elements. *Nat. Nanotechnol.* **20**, 523–531 (2025).
34. Wang, K. et al. Unambiguous discrimination of all 20 proteinogenic amino acids and their modifications by nanopore. *Nat. Methods* **21**, 92–101 (2023).
35. Wang, Y. et al. Identification of nucleoside monophosphates and their epigenetic modifications using an engineered nanopore. *Nat. Nanotechnol.* **17**, 976–983 (2022).
36. Wang, K. et al. Simultaneous identification of major thyroid hormones by a nickel immobilized biological nanopore. *Nano Lett.* **24**, 305–311 (2023).
37. Ouyang, Y., Wang, K., Jia, W., Zhang, P. & Huang, S. Simultaneous identification of vitamins B1, B3, B5, and B6 by an engineered nanopore. *Nano Lett.* **24**, 11944–11953 (2024).
38. Zhang, S. et al. A nanopore-based saccharide sensor. *Angew. Chem. Int. Ed.* **61**, e202203769 (2022).
39. Jeong, H., Byeon, E., Kim, D.-H., Maszczyk, P. & Lee, J.-S. Heavy metals and metalloid in aquatic invertebrates: a review of single/mixed forms, combination with other pollutants, and environmental factors. *Mar. Pollut. Bull.* **191**, 114959 (2023).
40. Kaushik, P., Khandelwal, R., Rawat, N. & Sharma, M. K. Environmental hazards of heavy metal pollution and toxicity: a review. *Flora Fauna* **28**, 315–327 (2022).
41. Bjerregaard, P., Andersen, C. B. I. & Andersen, O. in *Handbook on the Toxicology of Metals* (eds Nordberg, G. F. & Costa, M.) 593–627 (Academic Press, 2022).
42. Feng, Y., Teo, W. K., Siow, K. S., Tan, K. L. & Hsieh, A. K. The corrosion behaviour of copper in neutral tap water. Part I: corrosion mechanisms. *Corros. Sci.* **38**, 369–385 (1996).
43. Zhang, M., Sun, X., Hu, Y., Chen, G. & Xu, J. The influence of anthropogenic activities on heavy metal pollution of estuary sediment from the coastal East China Sea in the past nearly 50 years. *Mar. Pollut. Bull.* **181**, 113872 (2022).
44. Huang, S. The machine learning code designed for direct nanopore based divalent metal ion sensing. *Figshare* https://doi.org/10.6084/m9.figshare.30102343.v1 (2025).

Acknowledgements

The authors acknowledge Y. Du (Changchun Institute of Applied Chemistry, Chinese Academy of Science) for her assistance in the collection of salt lake water samples. S.H. acknowledges the National Key R&D Program of China (grant no. 2022YFA1304602), the National Natural Science Foundation of China (grant nos. 22225405, 22534004 and 223B2402), the Fundamental Research Funds for the Central Universities (grant no. 020514380336), the State Key Laboratory of Analytical Chemistry for Life Science (grant no. 5431ZZXM2509), the China National Postdoctoral Program for Innovative Talents (grant no. BX20250087), the Jiangsu Funding Program for Excellent Postdoctoral Talent (grant no. 2025ZB212) and the Yachen foundation of Nanjing University.

Author contributions

S.H. and W.S. conceived the project. W.S. and K.W. prepared the MspA nanopores. W.S., T.L., Z.W. and Y.X. performed the measurements. P.Z. set up the instruments. S.H. and W.S. wrote the paper. S.H. supervised the project.

Competing interests

S.H. and K.W. have filed patents describing the preparation of heterogeneous MspA and its applications (Application no. PCT/CN2022/124008, National Intellectual Property Administration, China). The remaining authors declare no competing interests.

Additional information

Extended data is available for this paper at https://doi.org/10.1038/s44221-025-00544-2.

Supplementary information The online version contains supplementary material available at https://doi.org/10.1038/s44221-025-00544-2.

Correspondence and requests for materials should be addressed to Shuo Huang.

Peer review information *Nature Water* thanks Xiyun Guan and Xiaofeng Kang for their contribution to the peer review of this work.

https://doi.org/10.1038/s44221-025-00544-2

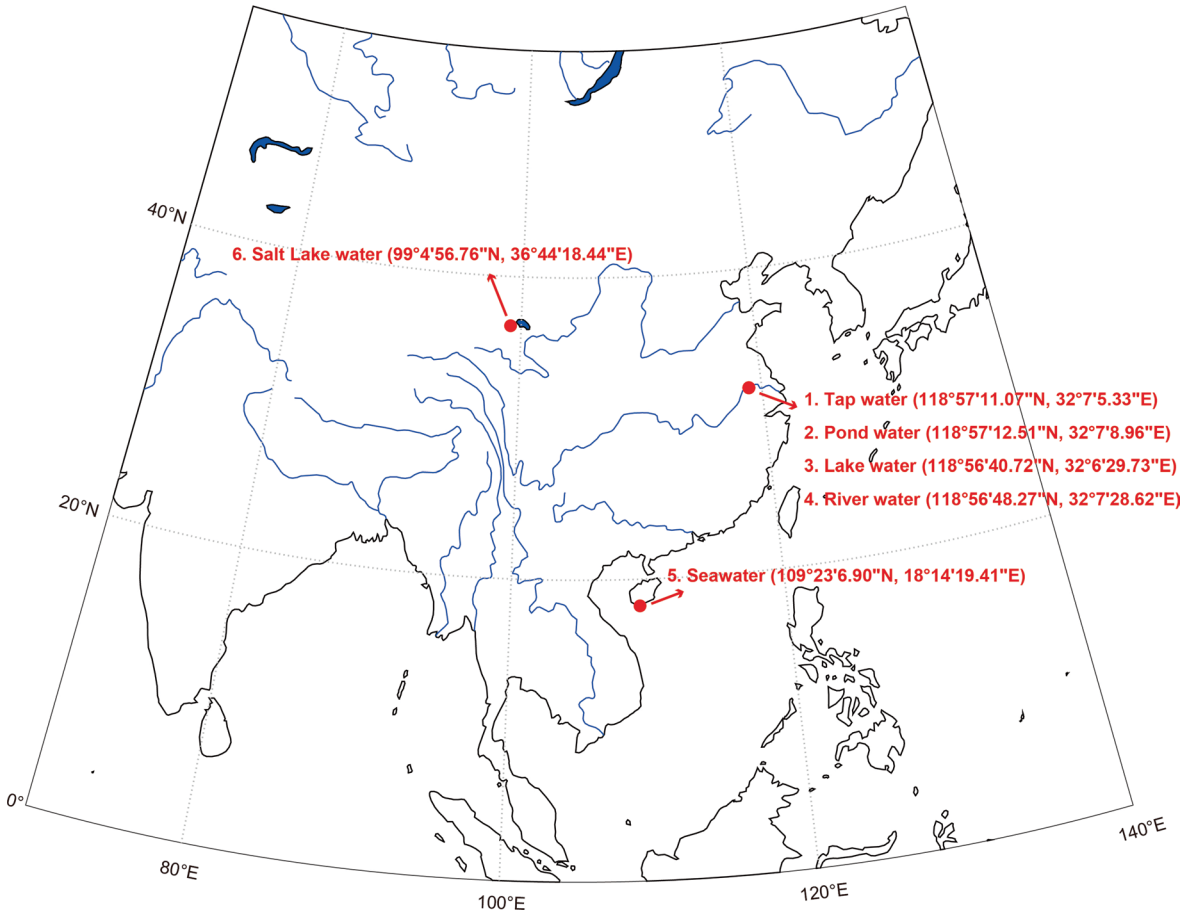

Extended Data Fig. 1 | A sampling location map. Geographic coordinates (longitude and latitude) are annotated on the axes. The sampling locations of six water samples are indicated on the map, with their specific latitude and longitude coordinates. Basemap generated using the Mapping Toolbox in MATLAB (Mathworks) under license number 40821794.

nature portfolio

Corresponding author(s): Shuo Huang

Last updated by author(s): Oct 23, 2025

Reporting Summary

Nature Portfolio wishes to improve the reproducibility of the work that we publish. This form provides structure for consistency and transparency in reporting. For further information on Nature Portfolio policies, see our Editorial Policies and the Editorial Policy Checklist.

Statistics

For all statistical analyses, confirm that the following items are present in the figure legend, table legend, main text, or Methods section.

n/a	Confirmed
☐	☒ The exact sample size (*n*) for each experimental group/condition, given as a discrete number and unit of measurement
☐	☒ A statement on whether measurements were taken from distinct samples or whether the same sample was measured repeatedly
☒	☐ The statistical test(s) used AND whether they are one- or two-sided *Only common tests should be described solely by name; describe more complex techniques in the Methods section.*
☒	☐ A description of all covariates tested
☒	☐ A description of any assumptions or corrections, such as tests of normality and adjustment for multiple comparisons
☐	☒ A full description of the statistical parameters including central tendency (e.g. means) or other basic estimates (e.g. regression coefficient) AND variation (e.g. standard deviation) or associated estimates of uncertainty (e.g. confidence intervals)
☒	☐ For null hypothesis testing, the test statistic (e.g. *F*, *t*, *r*) with confidence intervals, effect sizes, degrees of freedom and *P* value noted *Give P values as exact values whenever suitable.*
☒	☐ For Bayesian analysis, information on the choice of priors and Markov chain Monte Carlo settings
☒	☐ For hierarchical and complex designs, identification of the appropriate level for tests and full reporting of outcomes
☒	☐ Estimates of effect sizes (e.g. Cohen's *d*, Pearson's *r*), indicating how they were calculated

Our web collection on statistics for biologists contains articles on many of the points above.

Software and code

Policy information about availability of computer code

Data collection	Single channel recordings were performed by using an Axopatch 200B patch-clamp amplifier coupled with a Digidata 1550B digitizer.
Data analysis	The machine learning code is on Figshare. Please refer to the provided link (https://figshare.com/articles/dataset/M_II_classifier/30102343?file=57852106) for download.

For manuscripts utilizing custom algorithms or software that are central to the research but not yet described in published literature, software must be made available to editors and reviewers. We strongly encourage code deposition in a community repository (e.g. GitHub). See the Nature Portfolio guidelines for submitting code & software for further information.

Data

Policy information about availability of data

All manuscripts must include a data availability statement. This statement should provide the following information, where applicable:

- Accession codes, unique identifiers, or web links for publicly available datasets
- A description of any restrictions on data availability
- For clinical datasets or third party data, please ensure that the statement adheres to our policy

A set of demo events were accompanied for code validation. All other data presented in this work can be provided by the corresponding authors upon reasonable requests.

Research involving human participants, their data, or biological material

Policy information about studies with human participants or human data. See also policy information about sex, gender (identity/presentation), and sexual orientation and race, ethnicity and racism.

Reporting on sex and gender	N.A.
Reporting on race, ethnicity, or other socially relevant groupings	N.A.
Population characteristics	N.A.
Recruitment	N.A.
Ethics oversight	N.A.

Note that full information on the approval of the study protocol must also be provided in the manuscript.

Field-specific reporting

Please select the one below that is the best fit for your research. If you are not sure, read the appropriate sections before making your selection.

☐ Life sciences ☐ Behavioural & social sciences ☒ Ecological, evolutionary & environmental sciences

For a reference copy of the document with all sections, see nature.com/documents/nr-reporting-summary-flat.pdf

Ecological, evolutionary & environmental sciences study design

All studies must disclose on these points even when the disclosure is negative.

Study description	A custom developed novel nanopore sensor is used for direct analysis of divalent metal ions in natural water samples. The aim is to testify the technical validity of this newly developed nanopore sensor and to probe its potential for natural water sample analysis.
Research sample	The samples used in this study include representative natural water samples including sea water, river water, pond water, salt lake water and tap water. More details are described in the manuscript.
Sampling strategy	All data collected were included in the analysis.
Data collection	Data collection was performed by custom developed nanopore sensor platform.
Timing and spatial scale	Tap water, pond water, lake water, and river water samples were collected in Nanjing, China, on March 10, 2024. Seawater was sampled from Xidao, Sanya, China, on February 11, 2024, while salt lake water was collected from Caka Salt Lake, Qinghai, China, on August 4, 2024. Among these samples, tap water was obtained directly from a faucet in the university laboratory; the other five water types were all collected at a depth of 0.5 meters. The detailed sampling locations of all six water samples, including their specific latitude and longitude coordinates, are shown on a map (Extended Data Fig. 1).
Data exclusions	No data were excluded.
Reproducibility	All results were independently performed for at least 3 times to guarantee the reproducibility.
Randomization	No randomization was conducted.
Blinding	No blinding was conducted.

Did the study involve field work? ☐ Yes ☒ No

Reporting for specific materials, systems and methods

We require information from authors about some types of materials, experimental systems and methods used in many studies. Here, indicate whether each material, system or method listed is relevant to your study. If you are not sure if a list item applies to your research, read the appropriate section before selecting a response.

Materials & experimental systems

n/a	Involved in the study
☒	☐ Antibodies
☒	☐ Eukaryotic cell lines
☒	☐ Palaeontology and archaeology
☒	☐ Animals and other organisms
☒	☐ Clinical data
☒	☐ Dual use research of concern
☒	☐ Plants

Methods

n/a	Involved in the study
☒	☐ ChIP-seq
☒	☐ Flow cytometry
☒	☐ MRI-based neuroimaging

Plants

Seed stocks	N.A.
Novel plant genotypes	N.A.
Authentication	N.A.